*Particle Accelerators*, Vol. 63, pp. 171–210
Reprints available directly from the publisher
Photocopying permitted by license only



# EXPERIMENTAL INVESTIGATION OF ELECTRON COOLING AND STACKING OF LEAD IONS IN A LOW ENERGY ACCUMULATION RING

J. BOSSER, C. CARLI, M. CHANEL, C. HILL, A. LOMBARDI, R. MACCAFERRI, S. MAURY, D. MÖHL*, G. MOLINARI, S. ROSSI, E. TANKE, G. TRANQUILLE and M. VRETENAR

*PS Division, CERN, CH-1211 Geneva 23, Switzerland*

*(Received 3 May 1999; In final form 21 June 1999)*

This report gives the results of a programme of experimental investigations, which were carried out to test stacking of lead ions in a storage ring (the former Low Energy Antiproton Ring, LEAR) at 4.2 MeV per nucleon. The motivation was to demonstrate the feasibility of gaining the large factor in the phase-space density required for injection into the Large Hadron Collider (LHC). In the first part of the report, the layout of the experiments is described, the choice of the parameters of the electron cooling system used for stacking is reported and the multiturn injection using horizontal- and longitudinal- (and in the final project also vertical-) phase space is discussed. In the second part the experimental results are presented. Factors of vital importance are the stacking efficiency, the beam life-time and the cooling time of the ions. The beam decay owing to charge exchange with the residual gas and to recombination by the capture of cooling electrons was intensively studied. Beam instabilities and space–charge effects in the ion beam turned out to be additional, although less serious, limitations of the accumulation rate. The cooling speed as a function of cooler and storage-ring properties was investigated over a wide range of parameters. Among the 'surprises' encountered are an anomalously fast recombination rate for certain ion charge states ($Pb^{53+}$), a strong dependence of the cooling time on the dispersion function of the storage ring, and an intensity-dependent outgassing of equipment in the vacuum chamber. After a careful choice of parameters and antidotes, an overall factor of 120 in intensity could be gained, by multi-turn injection and stacking for 4 s. The intensity obtained ($6 \times 10^8$ ions with a length corresponding to four LHC bunches) is only a factor of two short of the LHC requirement, and the stacking time (4 s instead of 2 s foreseen for filling each LHC ring in 8 min) is another factor of 2 off.

*Keywords:* Beam cooling; Heavy-ion accelerators; Injectors

* Corresponding author. E-mail: Dieter.Mohl@cern.ch.

## 1 INTRODUCTION

In addition to proton–proton operation, the future Large Hadron Collider (LHC)[1] at CERN will work with heavy ions. In fact lead-ion collisions with an energy of 2.76 TeV/nucleon per beam are included in the conceptual design study[1] and other ions are also being discussed.[2]

One difficulty when colliding heavy ions at ultra-high energies is due to electromagnetic effects that cause disintegration or change of charge of the ions during the beam–beam interaction. They lead to a beam decay rate, which increases with the luminosity. Since a life-time of at least 6 h is required, this limits the luminosity to $2 \times 10^{27}\,\mathrm{cm}^{-2}\,\mathrm{s}^{-1}$. With reasonable assumptions on beam size and lattice parameters one then arrives at an intensity of $10^8$ ions per bunch.[1]

Although this is much lower than the $10^{11}$ particles per bunch required in proton operation, present day ion sources cannot directly deliver the corresponding phase-space density. To gain the missing factor of about 100, a scheme has been proposed,[3] where the ions are accumulated at low energy in a small storage ring with electron cooling. Starting at the end of 1994, a programme of tests was performed to investigate the techniques required for lead-ion cooling and stacking at the Low Energy Antiproton Ring (LEAR).[4] Only short exploratory runs were possible in 1994/1996. After the completion of the antiproton programme, at the end of 1996, LEAR was modified for more extensive tests including multiturn injection into longitudinal and transverse phase planes and accumulation with the help of electron cooling. The present paper describes the results of the full series of tests and draws conclusions for the future.

## 2 PARAMETERS OF THE EXPERIMENTS

### 2.1 Layout

The scheme[3] proposed for the LHC including the part tested so far is sketched in Figure 1. The existing ion source and linac were made use of: Lead ions of charge state 27+ from an Electron Cyclotron Resonance source (ECR) are accelerated in a linac section with RF-Quadrupole focusing (RFQ) and subsequently in a three-tank linac with Interdigital H structure (IH linac) to 4.2 MeV/nucleon. A stripping foil after the

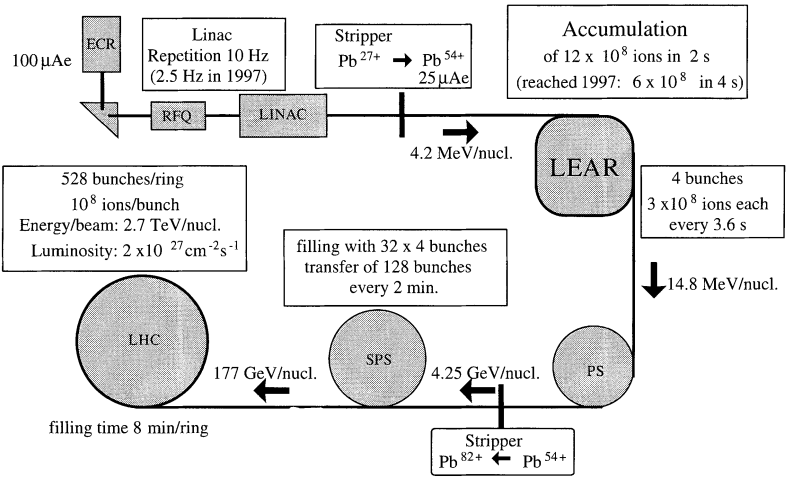


FIGURE 1 Sketch of the lead-ion injection scheme for the LHC. Required performance figures and, in brackets, performances of Linac 3 and LEAR obtained in the tests in 1997.

linac generates a distribution of charge states with a flat maximum around $Pb^{53+}$ and a conversion efficiency of about 16% for each single charge state in the range of 52+ to 54+. The desired state (e.g. $Pb^{54+}$) is then selected by a magnetic filter line ('dog leg') and transferred to the subsequent machine.

This arrangement (the lead ion 'Linac 3'[5,6]) has been used since 1994 to inject lead ions via the PS-booster and the PS into the SPS for fixed-target experiments at energies up to 177 GeV/nucleon. Linac 3 is housed in the location of the former Linac 1 used from 1982 to 1993 to inject test protons into LEAR.[4] The branch-off from the linac-booster transfer line was preserved to be able to inject ions from Linac 3 into LEAR for the tests and possibly also for the LHC.

## 2.2 Basic Beam and Electron Cooling Parameters

Experiments were performed with lead ions of four different charge states, $Pb^{52+}$ to $Pb^{55+}$. When it became clear that $Pb^{54+}$ had favourable qualities (see below) most tests were focused on this ion state. Some comparative measurements were also done with 50 MeV protons injected from a different linac ('Linac 2'). The basic beam and electron-cooling parameters are compiled in Table I.

TABLE I Main parameters of the lead-ion beam, the proton beam used in some complementary tests, and the corresponding electron-cooling beams

| | *Lead ions* | *Protons* |
|---|---|---|
| Kinetic energy | 4.2 MeV/nucleon | 50 MeV |
| Velocity factor $\beta = v/c$ | 0.095 | 0.31 |
| Storage-ring circumference $2\pi R$ | 78.54 m | 78.54 m |
| Kinetic energy of cooling electrons | 2.3 keV | 27 keV |
| Cooling length $\ell_c$ | | |
| until end 1996 | 1.5 m | 1.5 m |
| during 1997 | 3 m | 3 m |
| Electron-beam radius $a_e$ | 25 mm | 25 mm |
| Typical electron current $I_e$ | 0.05–0.4 A | 1–2.2 A |
| Magnetic field in cooler $B$ | 0.06 T | 0.06 T |

## 2.3 The Electron-Cooling Device

The LEAR electron-cooling device was recuperated from the Initial Cooling Experiment (ICE) performed in 1977–1979. For installation in LEAR the interaction length was shortened from 3 to 1.5 m and several improvements (e.g. a new 30 kV power supply and new compensation solenoids to cancel the coupling introduced by the main solenoid) were initiated in a collaboration with Kernforschungszentrum Karlsruhe (KfK) and further pursued by the LEAR-team. Later a new collector and a variable-intensity electron gun were constructed by a collaboration with CAPT-Lipetsk (Russia) and installed in LEAR.

The new gun[7] employs three electrodes: the Pierce shield, the grid, and the anode. It uses an adiabatic optics scheme in order to produce high intensity electron beams with low angular spread. The electron current density is controlled through the voltage on the grid electrode. One problem encountered in the production of dense beams is due to the storage of secondary electrons when the grid potential is positive with respect to the anode. This induces a reduction of the nominal electron current and also creates instabilities in the beam. At an energy of 2.3 keV, up to 1 A of electron current was obtained by pulsing the grid-to-anode potential to 0 V for about 1 μs. This empties the 'trap' present at the cathode level and restores the nominal current. However, as the trap refills with secondary electrons, pulsing of the grid potential was repeated every 100 ms. This procedure, together with a feedback system to cure the electron-beam instability, is described in detail in Ref. [8]. The ion cooling experiments were performed with electron currents

smaller than 0.5 A and, at this level, the instability could be efficiently controlled.

In 1994, a new two-year collaboration with the Russian team (which had moved to JINR Dubna) was set up to study the influence of neutralization of the electron beam. To this end, several electrodes were installed in the LEAR cooler to measure and control the state of neutralization. Also the vacuum chamber was modified to avoid the unwanted 'natural neutralization' of the electron beam. During the early stage of the lead-ion tests the influence of neutralization was explored,[9] but for the stacking tests during 1997 the neutralization level was chosen to be zero (see Section 3 below).

## 2.4 LEAR Lattices and Machine Modifications

The basic LEAR lattice[4] has four-fold symmetry with the same optical properties in all four long straight sections (Figure 2). Focusing is achieved by 16 quadrupoles (eight doublets) grouped into two families: All F-lenses (adjacent to the long straights) are powered in series by one supply and all D-lenses are powered by a second supply. Later four trimming supplies were added, providing the possibility of different currents in two F- and two D-subgroups. Originally used to create a

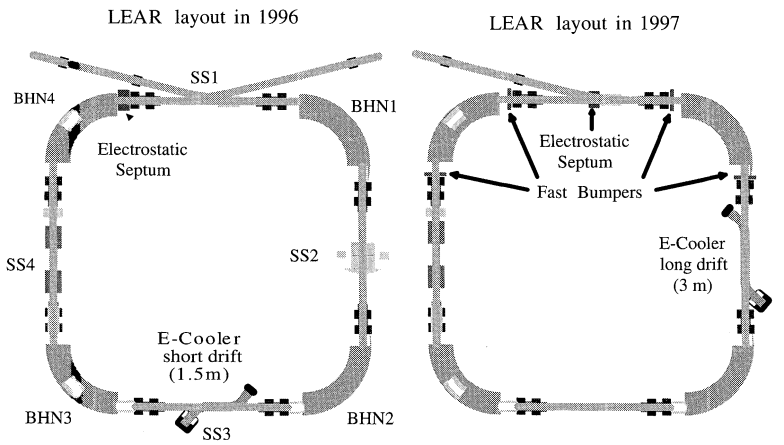


FIGURE 2 Configuration of LEAR in 1996 and modifications for the ion accumulation tests in 1997.

low-beta/zero-dispersion region in SS2 for internal target operation with antiprotons, the flexibility with a total of six families was used in the ion tests to explore the influence of the optics on electron cooling and on multiturn injection.

A detailed study[10] has shown that it is difficult to provide the widely different optical functions desired for injection and cooling in two straight sections on opposite sides of LEAR (like SS1 and SS3, where injection and electron cooling respectively were located for antiproton operation). Reasonable solutions rather tend to require two-fold symmetry or at least a 'pseudo-symmetry' with one set of properties in SS1/SS3 and a different set in SS2/SS4.

To 'decouple' cooling from injection, the electron cooling device was transferred, in 1997, from SS3 to SS2 (Figure 2). At the same time, advantage was taken of the increased space available after the removal of antiproton equipment. The interaction length of the cooler was increased from 1.5 to 3 m, in order to test the concurrent change of cooling speed and other properties like space–charge and ion–electron recombination behaviour. Further, to facilitate multiturn injection, the thin electrostatic septum, used up to the end of 1996 for the ultra-slow extraction of antiprotons, was moved to the centre of SS1 and four bumper magnets were installed to create the local orbit bump for injection (see Subsection 2.5.4 below). This conversion to a Low Energy Ion Ring (LEIR) opened the road to almost 'full scale' tests of the combination of multiturn injection and accumulation with the aid of cooling. Prior to the reconfiguration, only single-turn injection had been possible and it was necessary to accept optical functions at the injection septum, in SS1, which were closely associated with those to be tested at the cooler, in SS3. All together some 10 different optical settings were explored: machines 1 to 7 in 1994–1996; machine 1, and machines 97-0, 97-1 and 97-2 in 1997 (see Table II).

## 2.5 Multi-injection

### *2.5.1 Principle*

Both the transverse and the momentum acceptances of LEAR/LEIR are much larger than the corresponding properties of the beam from the linac (Table III). It is therefore advantageous to exploit the transverse

TABLE II Lattice functions for the optical settings of LEAR used in the experiments

| | | *Machines used up to 1996 (Machine no.)* | | | | *Machines used in 1997 (Machine no.)* | | |
|---|---|---|---|---|---|---|---|---|
| | | 1 | 4 | 6 | 7 | 97-0 | 97-1 | 97-2 |
| Twiss parameters at injection septum | $\beta_H$ [m] | 1.9 | 9.5 | 0.65 | 4.8 | 3.7 | 3.0 | 2.2 |
| | $\beta_V$ [m] | 6.4 | 10.5 | 5.5 | 5.0 | 6.5 | 6.6 | 6.3 |
| | D [m] | 3.6 | 0 | 0 | 5.0 | 10 | 9.9 | 9.5 |
| Twiss parameters at electron cooler | $\beta_H$ [m] | 1.9 | 9.5 | 0.65 | 4.8 | 5.0 | 5.0 | 5.0 |
| | $\beta_V$ [m] | 6.4 | 10.5 | 5.5 | 5.0 | 5.0 | 5.0 | 5.0 |
| | D [m] | 3.6 | 0 | 0 | 5.0 | 0 | −1.0 | −2.0 |
| Twiss parameters maximal values | $\beta_H$ [m] | 11.2 | 13.6 | 28.7 | 16.0 | 20.5 | 21.6 | 25 |
| | $\beta_V$ [m] | 22.7 | 21.8 | 26.9 | 25.2 | 20.2 | 20.9 | 21.5 |
| | D [m] | 3.6 | 9.9 | 10.2 | 5.1 | 10 | 10.1 | 10 |
| Working point | $Q_H$ | 2.31 | 1.62 | 2.76 | 2.55 | 1.59 | 1.59 | 1.59 |
| | $Q_V$ | 2.62 | 2.42 | 2.72 | 2.70 | 2.57 | 2.57 | 2.57 |
| Transition | $\gamma_{tr}^2$ | −39 | 8.1 | 8.1 | −28 | 8.1 | 18 | −33 |

TABLE III Acceptances of LEAR, emittances of the lead-ion linac and matched lattice functions of the transfer line at the injection septum

| | | |
|---|---|---|
| LEAR acceptances (Machine 97-0) | | |
| Horizontal | $A_H$ [$\pi$ mm mrad] | 150 |
| Vertical | $A_V$ [$\pi$ mm mrad] | 40 |
| Momentum | $\Delta p/p$ [$10^{-3}$] | $\pm 4$ |
| Linac 3 beam | | |
| Hor. emittance [$(2\sigma)^2/\beta$] | $\epsilon_H$ [$\pi$ mm mrad] | 10 |
| Vert. emittance [$(2\sigma)^2/\beta$] | $\epsilon_V$ [$\pi$ mm mrad] | 10 |
| Momentum spread | $2\sigma_p/p$ [$10^{-3}$] | 0.5 |
| Optimum transfer line functions at septum (Machine 97-0) | | |
| Horizontal $\beta$-function | $\beta_{H,L}$ [m] | $\approx 2$ |
| Vertical $\beta$-function | $\beta_{V,L}$ [m] | 6.5 |
| Dispersion | $D_L$ [m] | 0 |

and the longitudinal space simultaneously for multiturn injection.[11] In the test, the combination of horizontal and longitudinal injection was explored. In the final project, additional advantage of the vertical space may be taken, by use of a special (inclined or corner) septum[12] or by horizontal/vertical coupling as pioneered at the PS-Booster.[13]

The combined horizontal/longitudinal injection involves ramping the linac energy synchronized with a deformation of the circulating beam orbit, similar to the bump used in normal horizontal multiturn injection. A relatively large value of the dispersion function of the ring at the

septum, together with a moderate value of the beta function, is required ($D_S \approx 10\,\text{m}$ and $\beta_{H,S} \approx 3\,\text{m}$ for the Linac 3 and LEAR parameters summarized in Table III). The corresponding optimum Twiss parameters of the transfer line at the septum are $D_L = 0$ and $\beta_{H,L} \approx 2\,\text{m}$. Simulation[14] shows that in these conditions 25 effective turns can be injected with an efficiency of 60%. In these calculations the horizontal emittance resulting from injection was limited to $50\pi$ mm mrad (instead of the full acceptance of $150\pi$ mm mrad) to facilitate fast electron cooling.

Schematically the injection proceeds as follows (see Figure 3): The stack is 'parked' with an average momentum deviation $\Delta p/p \approx -3 \times 10^{-3}$, and thus, at $D = 10\,\text{m}$, with a displacement of $D\Delta p/p \approx -30\,\text{mm}$ from the central orbit. Most of the time the central orbit coincides with the centre of the chamber ($x = 0$), but prior to a new injection an orbit bump of $+50\,\text{mm}$ at the septum brings the centre of the stack in the injection region to a position of $+20\,\text{mm}$. Now let the incoming beam have a momentum deviation $\Delta p/p_L \approx -1.5 \times 10^{-3}$. Then its closed orbit centre is at $+35\,\text{mm}$ ($D\Delta p/p_L + x_{\text{bump}}$). Much like in normal horizontal multiturn injection, four turns are injected around this closed orbit, into a

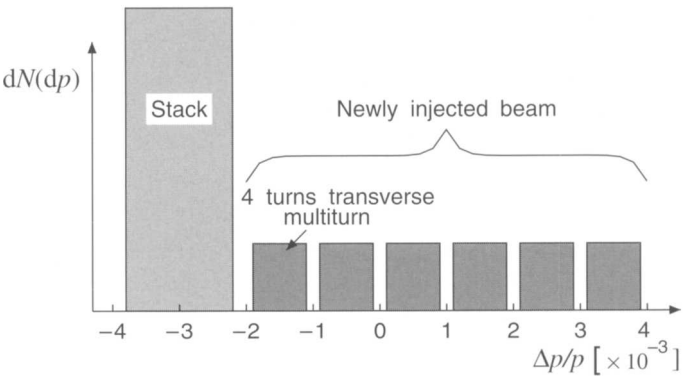


FIGURE 3 Representation of the combined longitudinal and horizontal multiturn injection in particle density vs. $\Delta p/p$-space. The stack is 'parked' with an average momentum deviation of $-3 \times 10^{-3}$ with respect to the centre of the chamber ($\Delta p/p = 0$). Schematically, four turns with an average $\Delta p/p = -1.5 \times 10^{-3}$ are injected into horizontal betatron space (usual multiturn injection). Then the average $\Delta p/p$ of the linac beam is 'switched' to $0.5 \times 10^{-3}$, the four-turn injection repeats and so on until the aperture limit at $\Delta p/p = 1.4 \times 10^{-3}$ is reached. In reality the momentum change is continuous rather than in steps.

phase-space area of about $50\pi$ mm mrad. Then the orbit bump is 'stepped down' from 50 to 40 mm so that the first turn, which would otherwise start to scrape the septum, avoids it. At the same time the linac momentum is stepped up by $1 \times 10^{-3}$ to $-0.5 \times 10^{-3}$, so that the closed orbit for the newly injected beam remains at 35 mm, four new turns are injected and this process is repeated until the last four turns are accepted with $\Delta p/p_L \approx +3.5 \times 10^{-3}$ and $x_{bump} = 0$. In reality the bump and the linac momentum change (approximately) linearly (see Figure 4) rather than in a staircase fashion with time, but the above schematization helps to understand the injection as a superposition of stacking in betatron and momentum phase space.

Electron cooling is used to merge the newly injected particles with the stack. The relatively small transverse emittance facilitates rapid cooling of the injected beam. In fact the above emittance and momentum parameters ($E_H \approx 50\pi$ mm mrad, $\Delta p/p \approx 7 \times 10^{-3}$ ramp plus stack) represent a good compromise between the number of particles injected and the cooling speed.

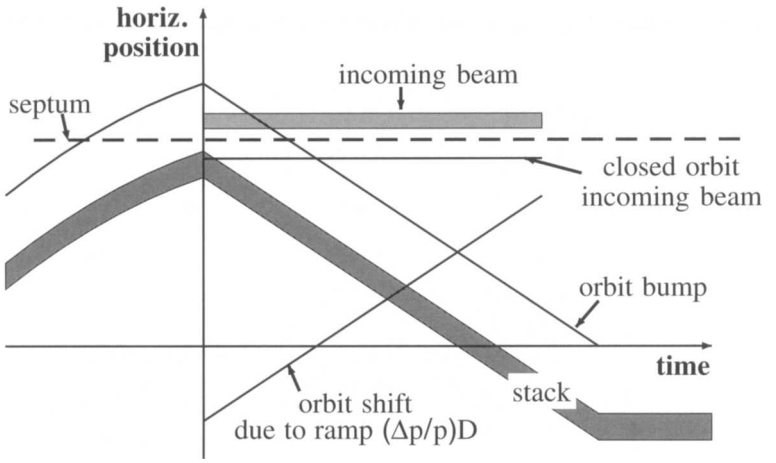


FIGURE 4 Orbit shift $[x_{bump}(t)]$ due to the bump, and $[D\Delta p/p_L(t)]$ due to the ramp of the linac momentum. Particles circulating (stack and injected turns) follow the displacement by the bump. For the incoming beam, $x_{bump}(t)$ and $D\Delta p/p_L(t)$ are arranged to cancel. Then the closed orbit for the arriving beam remains fixed and the incoming particles oscillate around this position. The amount of betatron space which is filled depends on the position of this orbit with respect to the incoming beam at the exit of the septum. Owing to the momentum ramping, the momentum acceptance is filled in addition to the betatron space.

### *2.5.2 Setting of the Transfer Line*

The line must have a sufficient momentum acceptance to accommodate the energy ramp ($\Delta p/p_L \approx 6 \times 10^{-3}$) plus the instantaneous momentum spread of the linac beam ($4\sigma_p/p \approx 1 \times 10^{-3}$). At the septum, the line must have zero dispersion, with a tolerance of $D \leq \pm 0.15$ m to ensure a displacement of less than $\pm 1$ mm during the ramp. A new optical setting of the transfer line was found,[15] which meets these requirements and at the same time provides the lattice functions at the injection septum, specified in Table III.

### *2.5.3 Ramping of the Linac Energy*

To change the output energy of the linac both the field (RF amplitude) of the last tank (tank3) and, linked to it, the RF phase of the debuncher cavity were changed dynamically during the beam pulse. This was achieved by adding two computer-controlled digital function generators which allowed flexible programming of the desired ramps.

In the final LHC injection scheme for lead ions, the linac beam pulse will have a repetition rate of 10 Hz. The source already pulses at this rate but other components need upgrading for such a fast cycle. In order to test a higher repetition rate than the 0.8 Hz used for standard operation, the RF and three quadrupoles in the linac–LEIR transfer line were run at 2.5 Hz. This was possible after minor modifications to the quadrupole power supplies. Higher repetition rates would require new quadrupole power supplies.

### *2.5.4 The Orbit-bump System*

The orbit excursion is created by four fast bumper magnets.[16] They are of lumped inductance type with a ferrite core and can be viewed as double C-shape magnets with a four-turn back-leg winding on either side (as described in Ref. [16]). The bumpers are arranged symmetrically with respect to the centre of SS1 (septum position) and located in the short straight sections on either side of the bending magnets BHN1 and BHN4 (see Figure 2). This arrangement facilitates the generation of a local orbit bump with its maximum at the septum and (ideally) zero orbit excursion outside the bumper region. For the symmetric bump the two inner and the two outer bumpers have the same excitation currents

TABLE IV Setting of the bumpers to create a symmetric bump with the maximum at the septum

| *Optics* | *Current ratio* | *Kick for a bump of* 40 mm *amplitude* | |
|---|---|---|---|
| | *Inner/outer bumpers* | *Inner bumpers* | *Outer bumpers* |
| Machine 1 | 1000 A/280 A | 9.4 mrad | 2.7 mrad |
| Machine 97-0 | 460 A/460 A | 4.3 mrad | 4.3 mrad |

$I_i$ and $I_o$ respectively, except for a small delay given by the travel time of the particles which can usually be neglected. The ratio $I_i/I_o$ for different optical settings, together with other parameters,[14] is given in Table IV.

The bumper magnets are installed on ceramic vacuum chamber sections, 250 mm long and with a half aperture $h \times v = 70\,\text{mm} \times 35\,\text{mm}$ for the beam. A thin metal layer (10 ohms per square) on the inside keeps the beam coupling impedance small. Each bumper has its individual power supply and each can provide a maximum integrated field of 110 G m (deflection of 10 mrad for $Pb^{54+}$ at 4.2 MeV/nucleon), which is reached for an excitation current of 1060 A. The generators make use of lumped-element pulse-forming networks which are charged from a DC supply and discharged via appropriately timed main, dump and clipping thyratron switches. They provide a waveform with an approximately sinusoidal rise (one quarter of a sine wave) in about 8–40 μs. The fall time, used for injection, can be chosen as 15, 25, 70 or 200 μs, according to the need of the experiment.

## 2.6 Specific Instrumentation

Schottky signals were used to measure a large variety of beam properties. A longitudinal Schottky band, usually the one near the 100th harmonic ($f = nf_{rev} \approx 36\,\text{MHz}$), was used to observe the evolution of the momentum distribution and of the beam intensity. In this way both the momentum cooling and the life-time of the beam could be followed. The intensity assessment from the area of the Schottky band was especially important in the case of monoturn injection, where the number of lead ions was too low to be reliably measured by the beam-current transformer. Transverse Schottky bands [$(n \pm Q)\, f_{rev}$ usually around 20 MHz] were used to observe the evolution of the emittances. To complement these measurements and to obtain absolute emittance values, beam ionization profile monitors were used. They measure the

beam profile by detecting the ions created in the collisional ionization of the residual gas by circulating beam particles.[17] These ions are extracted, guided by electric and magnetic fields, and detected by position-sensitive channel plates.

Examples of an intensity measurement by analysis of the Schottky noise and of the beam width by the horizontal profile detector are given in Figures 5 and 6.

The diagnostics was interfaced to a PC-based data acquisition system[18] and all the relevant beam properties could be obtained and treated online and/or offline. Four residual gas analysers could also be accessed via the PC system for recording the vacuum quality.

In addition to the PC-based system the usual LEAR diagnostics[19] was used. Secondary emission grids and/or scintillator screens and fast transformers could be adapted to set up and monitor the beam in the transfer line. The electrostatic pickup system to observe the orbit around the machine and the circulating beam current transformer to

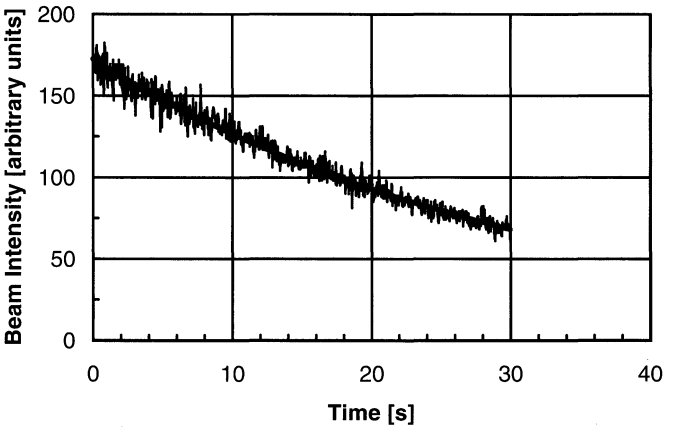


FIGURE 5 Example of a beam intensity vs. time measurement using the beam Schottky noise. The noise at the 100th harmonic ($f = 36$ MHz) of the revolution frequency is displayed, by means of a spectrum analyser used in receiver mode. The time evolution of the signal induced on a current pickup electrode is analysed. The total noise power in the band is recorded, by an appropriate choice of the resolution bandwidth of the analyser. The electronic noise of the acquisition adds in quadrature to the Schottky noise and has to be subtracted to obtain the Schottky power which is proportional to the ion beam current. The beam lifetime $\tau$ is obtained from an exponential fit $I = I_0 \exp(-t/\tau)$ to the $I(t)$ curve.

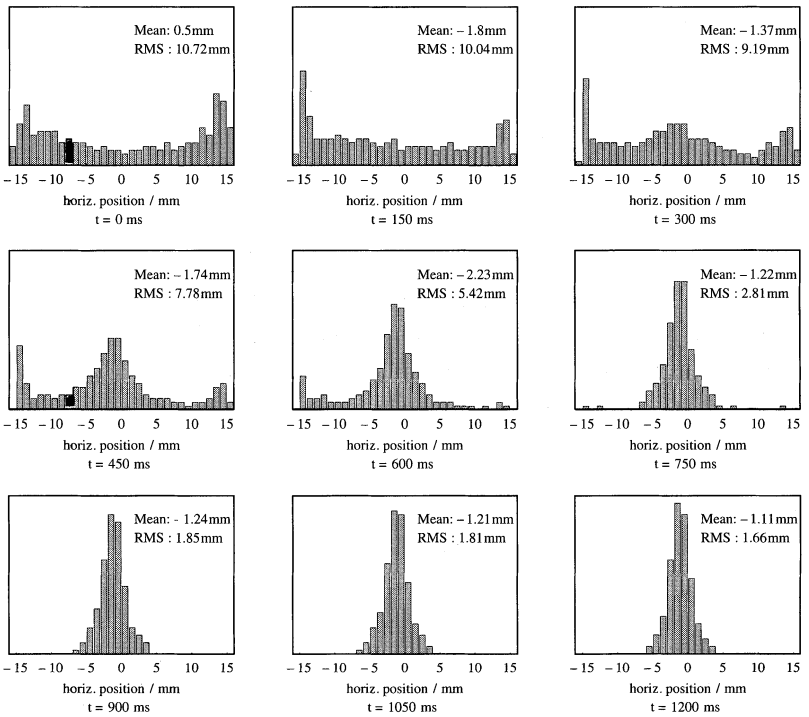


FIGURE 6 Example of the evolution of the horizontal profile of a $Pb^{54+}$ beam measured with the beam ionization profile monitor. The pictures were taken with machine 1, during electron cooling with $I_e = 47\,\text{mA}$ and a cooling length $\ell_c = 1.5\,\text{m}$.

monitor the intensity worked reliably once a figure of about $10^7$ ions was reached (i.e. after injection of a few turns).

## 3 COOLING AND LIFETIME MEASUREMENTS OF PARTIALLY STRIPPED LEAD IONS

### 3.1 Definition of Cooling Time

The cooling rate can be estimated from the simplified relation:[3,20]

$$\frac{1}{\tau} \approx 2.5 \times 10^{-13}\ [\text{Amp.}^{-1}\,\text{m}^2\,\text{s}^{-1}] \times \left(\frac{1}{R}\frac{q^2}{A}\frac{1}{\beta^4\gamma^5}\right) \times \ell_c j_e \frac{1}{\theta^3}. \quad (1)$$

Here 'fixed' parameters are the storage-ring mean radius ($R = 12.5$ m), the charge state and mass number ($q = 54$, $A = 208$), and the relativistic parameters ($\beta \approx 0.094$, $\gamma \approx 1$) of the ions. The 'variable' quantities are the current density $j_e$, defined as the electron current divided by the e-beam cross-section [in A/m$^2$], the length $\ell_c$ [m] of the cooling section and the r.m.s. angular spread $\theta$ [rad] between the ions and the electrons. For typical values (e.g. $\ell_c = 3$ m, $I_e = 0.1$ A, $a_e = 0.025$ m, $\theta = 0.004$–$0.005$ rad), Eq. (1) yields time constants ($\tau$) in the order of 0.1–0.2 s. The dependence of the cooling time on the 'variable' parameters was intensively investigated. In addition, the variation with the dispersion function, which does not explicitly appear in Eq. (1), was explored.

For comparative measurements, a clear definition of the cooling time is important. Throughout the experiments, the 'cooling-down time $\tau_h$' needed to reduce the horizontal emittance from $40\pi$ to $4\pi$ mm mrad was determined and used for comparison. Even then the horizontal cooling can still be influenced by the momentum spread and by the vertical emittance of the ion beam. Care was therefore taken to have similar starting values for $\Delta p/p$ and $\epsilon_v$ during each series of measurements. However the longitudinal cooling is usually much faster and the vertical emittance was small (frequently $\epsilon_v < 10\pi$ mm mrad) from the start so that most efforts were concentrated on the horizontal cooling. In all measurements, $(2\sigma)^2/\beta$ was used as emittance definition, where $\sigma$ is the square root of the variance of the measured profile and $\beta$ the value of the focusing function at the profile detector.

### 3.2 Cooling Time as a Function of Cooler Parameters

Figure 7 shows a compilation of cooling-rate measurements as a function of the electron current. In all measurements, great care was taken to align the electron and ion beams and to adjust the electron accelerating potential in order to ensure best possible conditions for fast cooling. One notices the linear increase, predicted by Eq. (1), of the cooling rate with electron current ($I_e$) up to about 100 mA, but for larger currents one can infer a tendency of 'saturation'. On the same graph one can see the effect of doubling the cooling length for the example of 'machine 1'.

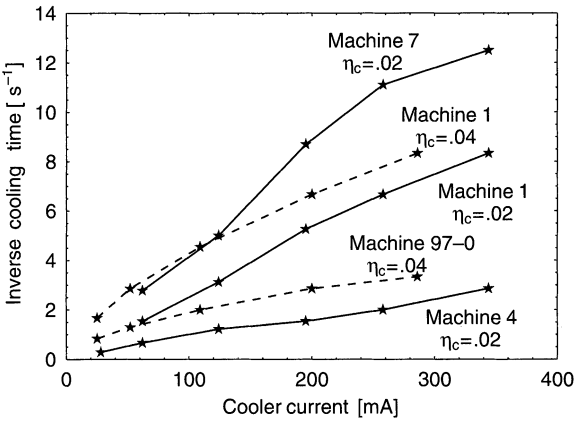


FIGURE 7 Cooling rate of $Pb^{54+}$ ions as a function of the electron-beam current for different lattice parameters and different lengths [$\eta_c = (\ell_c/2\pi R) = 0.02$, i.e. $\ell_e = 1.5$ m and $\eta_c = 0.04$, i.e. $\ell_c = 3$ m]. The values of the lattice parameters at the electron cooling device are given in Table II. The cooling rate is defined as the inverse of time needed to cool from a horizontal emittance $(2\sigma_H)^2/\beta_H$ of $40\pi$ down to $4\pi$ mm mrad. The initial vertical emittance and momentum spread were about $7\pi$ mm mrad and $0.5 \times 10^{-3}$ $(2\sigma_p/p)$ respectively.

Again for electron currents below 100 mA, the expected increase in cooling rate by a factor of two does show up. However for higher currents the gain is less pronounced. This may be explained by the effect of the electron space–charge, which is not included in Eq. (1). It introduces a variation of the accelerating potential $U$ with radial position ($r$). This dependence leads to a parabolic velocity profile of the electron beam: $v = v_0 + \Delta v(r)$ with $\Delta v(r) \propto r^2$. In fact for a uniform electron beam with a fractional neutralization $\eta_n$, radius $a_e$, and a vacuum pipe of radius $b$, the space–charge contribution to the potential (for $r \leq a_e$) and the concurrent velocity change are[21]

$$U_{sc} \approx 30\,\text{Volt} \times I_e\ [\text{Amp.}] \times \frac{(1-\eta_n)}{\beta}[r^2/a_e^2 - 2\ln(a_e/b) - 1],$$

$$\frac{\Delta v(r)}{v} = \frac{1}{\gamma(\gamma+1)}\frac{U_{sc}}{U} \approx \frac{1}{2}\frac{U_{sc}}{U}. \tag{2}$$

At 4.2 MeV/nucleon without neutralization, $\eta_n = 0$, and $I_e = 0.1$ A electron current, the velocity spread over the beam, $[\Delta v(a_e) - \Delta v(0)]/v$,

already amounts to $7 \times 10^{-3}$. This indicates that without special measures the cooling force near the border of the electron beam is considerably reduced. Then the cooling rate for the relatively large ion beam no longer increases linearly with the electron intensity. In addition tolerances for the alignment of the ion and electron beam become important, especially for the longer cooling section. Thus the observed 'levelling off' in the cooling both with electron intensity and cooling length can, at least qualitatively, be explained by the space–charge effect.

### 3.3 Cooling Time as a Function of Storage-ring Lattice

Special importance was attached to the dependence of the cooling time on the optical parameters of the storage ring. For given emittance and momentum spread, the lattice parameters $\beta$ and $D$ determine the size and the angular distribution of the ion beam. The cooling rate, Eq. (1), depends strongly on the angular spread $\theta$ between ions and electrons. When the average velocities are well matched then $\theta$ is simply given by the ion and electron spreads $\theta = \sqrt{\theta_i^2 + \theta_e^2}$, and as the ion angle has the contribution $\theta_{iH} = \frac{1}{2}\sqrt{\epsilon_H/\beta_H}$ one would expect that a large $\beta$-function at the cooler facilitates fast cooling (at least in the range where the ion angle $\theta_i$ is larger than the electron spread, which was $\theta_e = \sqrt{T_e/(mc^2\beta^2\gamma^2)} \approx 4$ mrad for the estimated electron temperature of $T_e = 0.1$ eV).

On the other hand, a large $\beta$-function implies a large ion beam ($a_{iH}^2 = \epsilon_H \beta_H$), and one expects a degradation of the cooling force once the ion beam becomes comparable in size to the electron beam. This degradation is due to the space–charge effect, Eq. (2), which tends to complicate the ion–electron velocity matching over a large beam size, and eventually also due to imperfect overlap when the ion beam is larger than the electron beam.

As a consequence one anticipates optimum conditions for intermediate values of the $\beta$-function (around 10 m in the experiments), which lead to an initial ion-beam size slightly smaller than the electron beam.

In the experiments, the dependence on the lattice functions was explored in detail with 50 MeV protons, which are easier to handle than

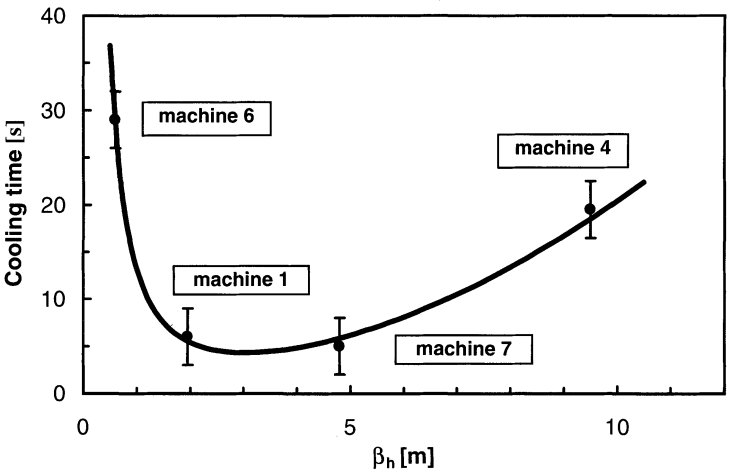


FIGURE 8 Plot of the proton-beam cooling time vs. horizontal beta function at the cooler. The electron current was 1.2 A and the cooling length 1.5 m. The measured time is the time needed to cool about $2 \times 10^9$ protons at 50 MeV from a horizontal emittance $(2\sigma_H)^2/\beta_H$ of $40\pi$ down to $4\pi$ mm mrad. The initial vertical emittance and momentum spread $(2\sigma_p/p)$ were about $10\pi$ mm mrad and $2 \times 10^{-3}$ respectively. The curve corresponds to a fit $\tau \approx 0.2\beta_H + 13/\beta_H^{3/2}$.

the lead ions. Figure 8 shows the result of cooling-time measurements, made in 1996, for four different optical settings. In this series the electron current was 1.2 A. By virtue of Eq. (2), this leads to the same relative space–charge effect $[U_{sc}(r)]/U$ at the higher energy as a current of 30 mA at 4.2 MeV/nucleon ions. One observes in Figure 8 the best cooling for $\beta$-values in the range of 2 to 5 m (machines 1 and 7), which is lower than expected. It should however be mentioned that, in addition to the difference in horizontal $\beta$-function, machines 1 and 7 have dispersion functions $D$ of about 3.5 and 5 m respectively, whereas machines 4 and 6 have zero dispersion at the cooler. It is clear then that the influence of $D$ is superimposed on the $\beta_H$-dependence and may even be the dominant effect. In the 1996 'antiproton configuration' of LEAR, we did not succeed in testing a setting with intermediate $\beta_H$-values and zero dispersion at the cooler.

Guided by the observations with protons, three optical settings (machines 1, 7 and 4) were tested with lead ions. In these measurement series the electron current was 350 mA. Therefore the relative

spread of the accelerating voltage due to space-charge $\Delta U/U = [U_{sc}(a_e) - U_{sc}(0)]/U \approx 5\%$ (see Eq. (2)), is more important than in the proton case ($\Delta U/U \approx 0.7\%$). Nevertheless the results (Figure 9) are similar and indicate that machine 7 is close to optimum and gives cooling-down times of less than 100 ms. However the relatively large dispersion at the cooler ($D = 5$ m) with this optical setting makes the multi-injection and stacking with a large momentum width difficult.

The influence dispersion can, at least qualitatively, be explained by reference to Figure 10, which displays the longitudinal velocity vs. horizontal position profiles for both the electrons [Eq. (2)] and the ions. For the latter, the 'working line' is given by the dispersion function $D$ as

$$\frac{\Delta v(x)}{v} = \frac{1}{\gamma^2}\frac{\Delta p}{p} = \frac{1}{D\gamma^2}x. \tag{3}$$

The shaded area around the dispersion line has its width given by the betatron oscillation and its height $(\Delta v/v)_{max} \approx \Delta p/(p)_{max}$ by the momentum bite of the ion beam. The cooling force increases when

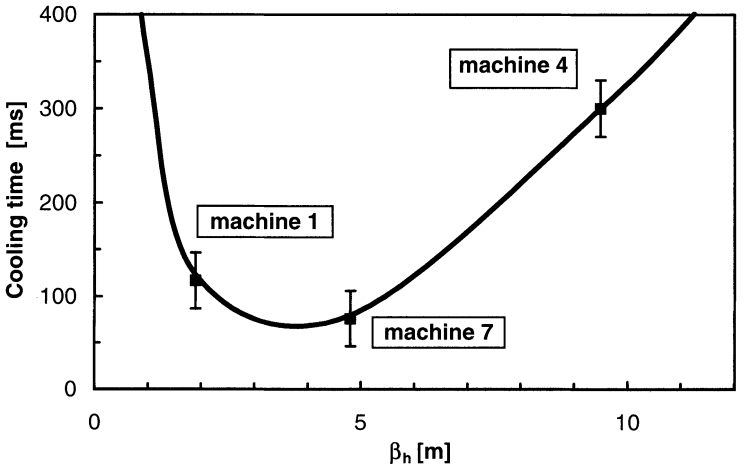


FIGURE 9 Cooling-down time for $Pb^{54+}$ ions at 4.2 MeV/nucleon vs. horizontal beta function. The electron current was 350 mA and the cooling length 1.5 m. Initial ion-beam properties and definition of cooling time as for Figure 7. The curve is drawn to guide the eye. It corresponds roughly to a fit $\tau \approx 3.2\beta_H + 230/\beta_H^{3/2}$.

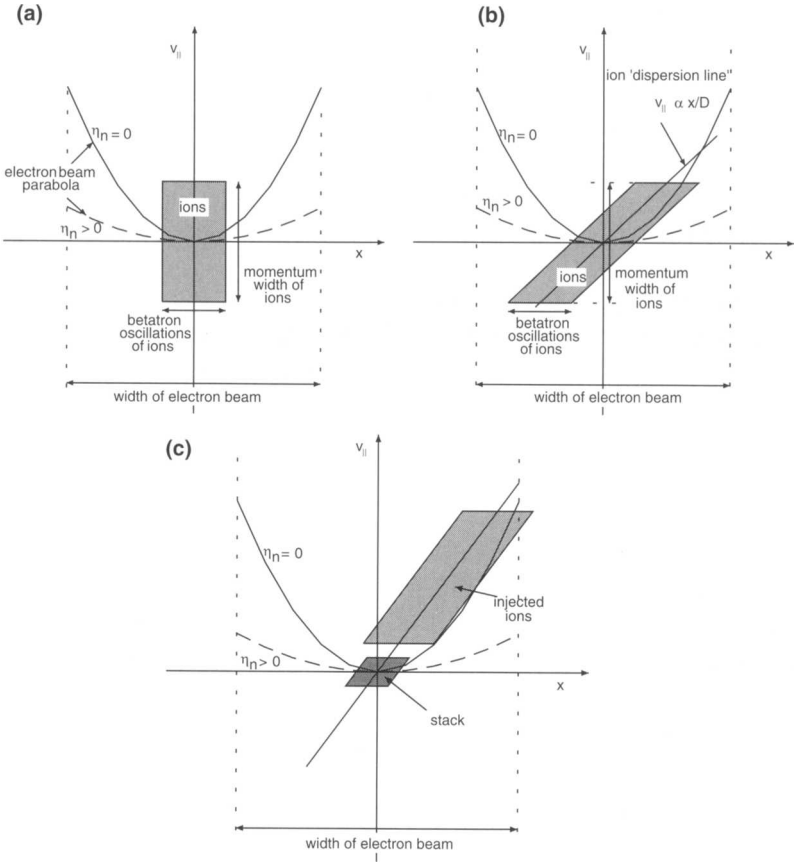


FIGURE 10 Velocity vs. horizontal position profile of the electron and ion beams. Owing to space–charge, the electron profile is a parabola, whereas the velocity of the ions varies linearly, with slope $1/D\gamma^2$, Eq. (3). For zero dispersion (a), the 'dispersion line' is vertical. For finite $D$, (b) and (c), it is inclined. Owing to their betatron oscillation, ions occupy the area (indicated by shading) around the dispersion line. The steepness of the parabola depends on the electron density and on the state of neutralization of the electron beam. With space–charge compensation, the parabola flattens and theoretically becomes a horizontal line for full neutralization. During cooling, the ion beam converges to the (first) intersection point of the dispersion line with the parabola. In (a) and (b), the electron energy is adjusted to match the average ion velocity. In (c), it matches the minimum ion velocity, which corresponds to the stack in the injection scheme described.

the distance $\Delta v$ between the ion orbit in $v, x$-space and the parabola decreases. In fact in the simple binary collision model, the friction force on an ion at position $x$ is proportional to $\{\vec{v}_i(x) - \vec{v}_e(x)\}/|v_i(x) - v_e(x)|^3$. For zero dispersion the difference $|v_i(x) - v_e(x)|$ is on average relatively

large. For finite dispersion the difference can be much smaller, but for large $x$, beyond the second intersection of the dispersion line with the parabola, $\{\vec{v}_i(x) - \vec{v}_e(x)\}$ becomes negative and ions in that range experience heating instead. Thus one expects fastest cooling for a value of the dispersion such that the ion working line 'matches the inside' of the electron parabola. In this matching, some margin has to be left for the betatron motion.

It is clear from this qualitative picture, that the optimum $D$-value depends on the electron current as well as on the ion momentum bite and, to some extent, also on the betatron width to be handled. Neglecting the betatron oscillation and accommodating the ion momentum spread in the way sketched in Figure 10(c), between the first and second intersection point of the dispersion line with the parabola [Eq. (2)], the optimum dispersion is obtained as

$$D \approx \sqrt{\frac{1}{30\Omega}\frac{\gamma+1}{\gamma}\frac{\beta U a_e^2}{I_e(\Delta p/p)_{\max}}}. \tag{4}$$

One can see from Figure 10(c) that in this case, and in particular for the 'stacking scheme' sketched, the beam is cooled to the lower end of the momentum bite rather than to the central momentum.

For the parameters used for stacking [with $(\Delta p/p)_{\max} = 10^{-2}$ 'stack + ramp + instantaneous spread'] Eq. (4) yields $D = 1.6$ m; but to leave room for betatron oscillations, a smaller value ($D = 0.5$ to 1 m) should be chosen. For the results summarized in Figure 9 the initial momentum spread was smaller, $(\Delta p/p)_{\max} \approx 6(\sigma_p/p) = 1.5 \times 10^{-3}$, and Eq. (3.4) suggests a somewhat larger dispersion ($D \approx 4$ m). Finally, for the measurements with protons shown in Figure 8, Eq. (4) predicts an optimum $D \approx 6$ m.

To investigate the influence of dispersion on the cooling time, a series of measurements was performed with protons using four different optical settings: the standard (machine 1) optics and the optics used for stacking (machine 97), for which the values $D = 0$, $-1$ and $-2$ m at the cooler could be adjusted with almost no change of the $\beta$-functions. Cooling-down times after single-turn injection were measured as a function of the offset in horizontal position between proton and electron

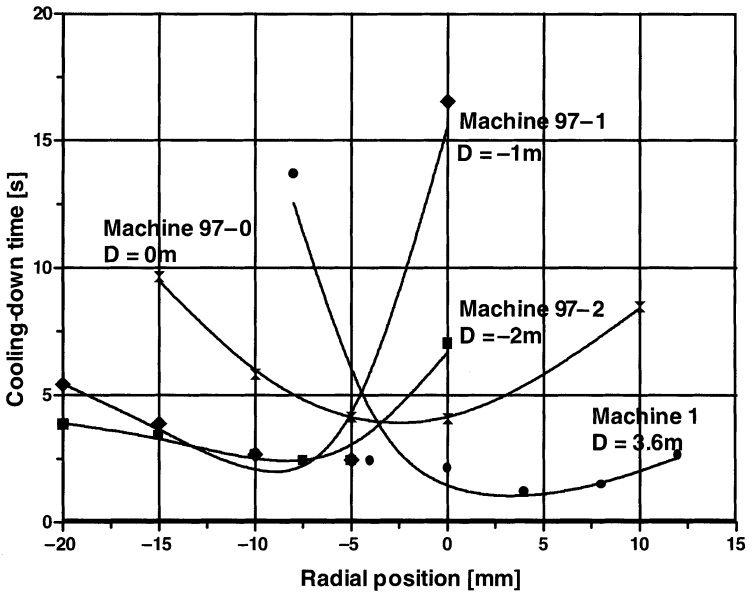


FIGURE 11 Cooling-down time for 50 MeV protons as a function of the horizontal offset between proton and electron beam for machine 1 and machines 97-0, 97-1 and 97-2. The electron current in this measurement series was 1.1 A and the cooling length was 3 m. Initial and final beam conditions are as for Figure 8.

beam. The electron current was $I_e = 1.1$ A and the 50 MeV proton beam had the following initial emittances (2 r.m.s.): $\epsilon_H = 40\pi$ mm mrad, $\epsilon_v \approx 10\pi$ mm mrad, $2\sigma_p/p \approx 2 \times 10^{-3}$. The results, shown in Figure 11, indicate quite clearly that the dispersion plays an important role. The fastest cooling times are obtained with settings that have finite dispersion in the cooling section. Because of the electron space–charge, cooling in the presence of dispersion no longer depends in a symmetric way on the ion–electron offset. For positive dispersion cooling is fastest for a positive offset and vice versa for negative $D$, as expected from examination of Figures 10(b) and (c). The curve for the case of zero dispersion is (within the precision of the measurement) symmetric about $\Delta x = 0$. One notes a factor of 2 slower cooling than for $D = 3.5$ m, but the range which can be exploited for cooling is larger ($\Delta x \approx -15$ to $+15$ mm for $D = 0$, compared to $\Delta x \approx -20$ to $-5$ mm for $D = -1$ m, Figure 11).

The difference between the curves measured for $D = -1$ and $-2$ m is not fully understood. However the extrapolation of the results to ions at 4 MeV/nucleon seems to confirm the conclusion that a lattice with a finite dispersion ($|D| \approx 1$ m) and a relatively small $\beta$-function ($\beta_H \approx 5$ m) at the cooler is well suited for the stacking scheme envisaged.

### 3.4 Test with a Neutralized Electron Beam

In addition to the modification of the accelerating potential discussed above [see Eq. (2)], the transverse component of the electron space–charge field, together with the external $B$-field of the cooler introduces an $(E \times B)$-drift of the electrons[9,22] with a drift velocity $v_d = [\partial U_{sc}/\partial r]/B\gamma^2$, where $U_{sc}$ is the space–charge potential given by Eq. (2). This drift velocity adds to the electron velocity spread and may further reduce the cooling speed. The neutralization experiments were aimed at eliminating this effect, together with the variation of the accelerating potential, by a uniform neutralization of the electron beam with a neutralization factor $\eta_n \approx 1$ [see Eq. (2)]. After it had become possible to work with stable neutralization levels that could be chosen between 0 and 1 for currents up to $I_e = 200$ mA at 2.3 keV electron energy, a series of tests was performed. The cooling time was measured at various different $\eta_n$ levels both for an optical setting with (machine 1) and without (machine 4) dispersion at the cooler. Results can be summarized by stating that no appreciable gain in cooling speed was obtained with neutralization.

One reason for this was the difficulty to obtain a uniform neutralization. Instead $\eta_n$ varied with radial position with a sharp decrease near the border of the electron beam. This was clearly visible (Figure 12) when the cooled ion beam was used as a 'pencil probe' to test the enhancement [Eq. (2)] of the accelerating potential by space–charge. In these measurements,[23] the horizontal position of the ion beam in the cooling section was varied by a local orbit displacement ($x$). For each $x$ the cathode potential was readjusted by an amount $\Delta U(x)$ such that the velocity (energy) of the ions remained the same as that previously measured in the centre ($x = 0$) of the electron beam. The cooled ions match the local electron velocity and thus $\Delta U(x)$ is a direct measure of the electron space–charge potential $\Delta U(x) = U_{sc}(x) - U_{sc}(0)$.

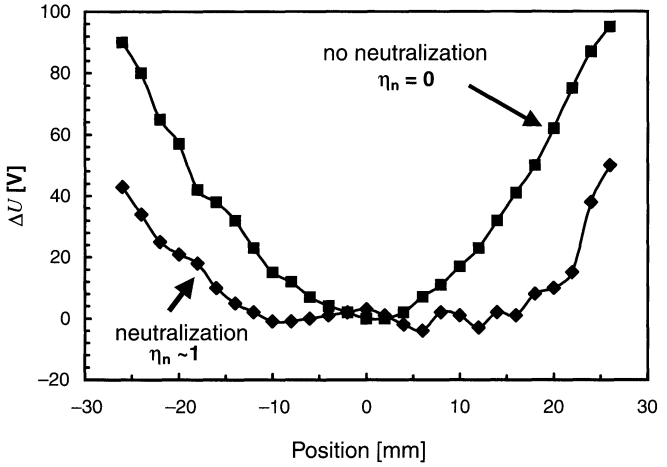


FIGURE 12 Change of the effective accelerating voltage $U$ with horizontal position in the electron beam. The 1 A beam with 25 mm radius is accelerated by an external potential of about 27.4 kV. Space–charge induces a shift $\Delta U(x)$ with respect to the beam centre. The potential is probed with a cooled proton beam displaced by a local orbit bump. Without neutralization, $\Delta U(x)$ is a parabola. With neutralization, $\Delta U(x)$ is flattened in the centre. The central value is adjusted to $\Delta U(0) = 0$ in both cases by retuning of the external potential.

The ion velocity was deduced from the revolution frequency observed via the Schottky noise according to the relation

$$\frac{\Delta f}{f} = (1 - \gamma^2/\gamma_{\mathrm{tr}}^2)\frac{\Delta v}{v} - \frac{\Delta \ell}{2\pi R}. \tag{5}$$

The fractional increase $\Delta\ell/(2\pi R)$ of the orbit length due to the local excursion is typically smaller than $10^{-5}$ so that by adjusting to $\Delta f = 0$ one obtains a good approximation of $\Delta v = 0$. Figure 12 shows an example of the space–charge potential $\Delta U(x)$ without and with neutralization measured in this way. The agreement with Eq. (2) is good, except at the edge of the electron beam where the potential rises steeply with a sizeable change over the width ($\approx 3$ mm) of the cooled ion beam. With neutralization, the profile $U(x)$ is flat in the centre, but rises towards the border of the electron beam, indicating that the neutralization is not uniform but varies with the radial position.

Another effect observed with neutralization was a marked reduction of the life-time for the lead-ion beam. This can be explained by charge exchange between the circulating beam and the neutralizing ions. In fact the density of the neutralizing ions is equivalent to a residual gas pressure $P_{eq}$, all around the ring, given by the circumference factor $\eta_c = \ell_c/2\pi R$ of the cooler, the neutralization factor $\eta_n$, and the density $n_e = I_e/\pi a_e^2 \beta ce$ of the electron beam:

$$P_{eq} = 3 \times 10^{-17} \text{ torr } \eta_c \eta_n n_e \text{ [cm}^{-3}\text{]}.$$

For $\eta_c = 0.02$, $\eta_n = 1$, $I_e = 200$ mA (i.e. $n_e = 2.3 \times 10^7$ cm$^{-3}$) this yields $P_{eq} = 1.3 \times 10^{-11}$ torr, which is higher than the normal LEAR vacuum pressure (about $5 \times 10^{-12}$ torr under static conditions, see Sections 3.5 and 3.7 below). This explains the fast beam decay, especially since it was found that the neutralizing ions have a relatively high mass.[24]

Because of this harmful effect and also because no clear improvement of the cooling time was found, the stacking tests were done without neutralization. However it was vital to stabilize the neutralization at a given level: zero in the present case. Any jump in $\eta_n$ did not only cause disturbing changes in the beam energy but also strong additional losses. To avoid unwanted 'natural' neutralization, the vacuum chamber was modified to present a uniform shield to the electron beam over the entire length. In this way, beam-induced potentials that can trap ions were avoided. In addition the 'shaker' electrodes[24,25] were used. They expel neutralizing ions by a transversely deflecting RF field with a frequency of some 100 kHz in the range of ion bounce frequencies in the electron beam.

### 3.5 Beam Decay due to Charge Exchange with the Residual Gas

The beam life-time was estimated by recording the intensity versus time. The decay rate

$$\frac{1}{\tau} = \frac{1}{\tau_{vac}} + \frac{1}{\tau_{rec}} \tag{6}$$

has contributions due to charge exchange with the residual gas ($1/\tau_{vac}$) and due to the presence of the electron beam ($1/\tau_{rec}$). The latter increases with the electron current, whereas the former is independent of $I_e$ and

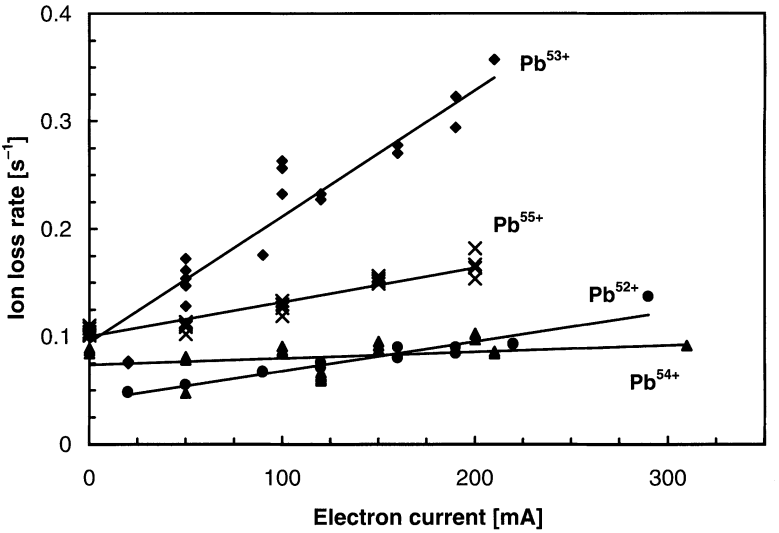


FIGURE 13 Dependence of the ion-beam decay rate on the electron cooling current for Pb charge states 52+ to 55+. The decay rate for $I_e = 0$ is determined by charge exchange with the residual gas. This process has practically the same cross-sections for the charge states investigated. The variation rather reflects different vacuum conditions in the different runs. From the slope of the $1/\tau$ vs. $I_e$ lines, rate coefficients can be determined. They describe the recombination rate with cooling electrons and perhaps other loss mechanisms proportional to the electron density.

depends on the residual-gas composition and pressure. Figure 13 shows a plot of $1/\tau$ versus $I_e$ for lead ions of charge states 52+ to 55+. From the intercept with the vertical axis ($I_e = 0$) the life-time due to the residual gas can be obtained. Depending on the vacuum conditions, lifetimes $\tau_{vac}$ in the range of 6–20 s were measured during the various runs. The vacuum pressure could be estimated from the reading of 15 pressure gauges distributed around the ring and the gas composition from four residual-gas analysers located in the four long straight sections. The measured values of $\tau_{vac}$ were in all cases in good agreement with the semi-empirical formula of Franzke [25], which estimates $\tau_{vac}$ for given vacuum conditions. For instance for a residual gas atmosphere consisting of about 82% $H_2$ and 18% heavier molecules like CO and $N_2$ with a composite pressure of $2.1 \times 10^{-11}$ torr, the calculated life-time is 15 s whereas 13 s were measured. No dependence of $\tau_{vac}$ on the charge state was observed, in agreement with the theory which predicts similar cross-sections for

the charge states tested. The measurements for different charge states were performed on different occasions, and the difference in $\tau_{vac}$ inferred from Figure 13 reflects the different vacuum conditions but not (very) different cross-sections.

### 3.6 Beam Decay due to Recombination with Cooling Electrons

The component $1/\tau_{rec}$ of the decay rate, which increases with the electron current, can be deduced from the slope of the curves in Figure 13.

A very strong dependence on the charge state can be observed. In fact the decay for $Pb^{53+}$ increases almost a factor of 10 faster with the electron current than for the neighbouring states. More results are summarized in Table V where rate coefficients $\alpha_{rec}$ are compiled. These coefficients give the slope of the decay rate $1/\tau_{rec}$ as a function of $n_{eff}$, where the effective electron density is given by the true density of the electron beam, reduced by the fraction $\eta_c$ of the circumference covered by the cooling section: $n_{eff} = n_e \eta_c$. For the LEAR cooler (Table I) at 2.3 keV electron energy one obtains

$$n_{eff} \approx 1.1 \times 10^6 (\text{cm}^{-3}\,\text{Amp}^{-1}) \times I_e \times \eta_c, \quad \eta_c \approx \begin{cases} 0.02 & \text{before 1997} \\ 0.04 & \text{during 1997.} \end{cases}$$

The following observations can be made from Table V. The rate coefficient for $Pb^{53+}$ is unusually high. Values close to $60 \times 10^{-8}\,\text{cm}^{-3}\,\text{s}^{-1}$ were measured in all runs, independent of the optical settings of LEAR. For $Pb^{52+}$ and $Pb^{55+}$ coefficients of the order of $10 \times 10^{-8}\,\text{cm}^{-3}\,\text{s}^{-1}$ were found. There are not enough measurements to discern a dependence on the lattice functions. Finally for $Pb^{54+}$, coefficients in the range

TABLE V Loss-rate coefficients measured for lead ions of different charge states and different machine settings

| *Run* | *Loss rate coefficient*/$(10^{-8}\,\text{cm}^{-3}\,\text{s}^{-1})$ | | | | *Machine no.* |
|---|---|---|---|---|---|
| | $Pb^{52+}$ | $Pb^{53+}$ | $Pb^{54+}$ | $Pb^{55+}$ | |
| Dec. 94 | | 64 | | | 4 |
| June 95 | 11 | 60 | 9 | | 1 |
| Dec. 95 | | 63 | 5 | 12 | 4 |
| Mar. 96 | | 60 | 9 | | 1 |
| ,, | | 60 | 6 | | 4 |
| ,, | | | 8 | | 7 |
| 1997 | | 60 | 7 | | 97-0 |

$5–9 \times 10^{-8}\,\mathrm{cm}^{-3}\,\mathrm{s}^{-1}$ were measured, apparently depending on the lattice functions at the cooler. For the interaction length of 3 m (instead of 1.5 m used before 1997) the same normalized rate coefficients $\alpha_{\mathrm{rec}}$ were measured, i.e. $1/\tau_{\mathrm{rec}}$ increases by two as expected.

The measured rate coefficients are not easily explainable by existing theory. Electron temperatures of 0.1–0.2 eV for radiative capture at the LEAR cooler were estimated from the $H^0$ rate, measured when protons were cooled. Then for $Pb^{52+}$ to $Pb^{55+}$, one expects radiative capture coefficients of the order of $2–3 \times 10^{-8}\,\mathrm{cm}^{-3}\,\mathrm{s}^{-1}$, which depend only weakly on the charge state. Rates up to 10 times faster than expected for radiative recombination had been reported for special, partially stripped ions in the literature prior to the LEAR measurements and attempts to explain them by dielectronic capture have been made (see [26] and references given therein). The same explanation could apply to $Pb^{52+}$, $Pb^{54+}$ and $Pb^{55+}$. However the rate for $Pb^{53+}$ points to an unusually strong capture resonance or other mechanisms. Recently a similar 'anomaly' was found at the TSR-Heidelberg for gold ions.[27] An unusually high rate coefficient (of the order of $100 \times 10^{-8}\,\mathrm{cm}^{-3}\,\mathrm{s}^{-1}$) was measured for $Au^{50+}$, which is isoelectronic with $Pb^{53+}$. Most measurement at LEAR were performed with a longitudinal magnetic field $B = 600$ G in the cooler. For $Pb^{53+}$ and $Pb^{54+}$, tests were also done with other $B$-values, but no significant dependence of $\alpha_{\mathrm{rec}}$ on the field was observed for the values ($B = 200–800$ G) accessible.

Several additional tests were performed to cross-check the conjecture that the loss in the presence of the cooling beam is indeed due to recombination of ions with cooling electrons. The energy of the electron beam was offset by a large amount. In this case, the life-time increased and reached a value which was independent of the charge state and only slightly shorter than in the absence of the electron beam. The difference can be explained by the pressure bump resulting from small losses from the electron beam. A second series of cross-checks used a movable scintillation screen. It was installed in the first bending magnet downstream of the cooling section to intercept the $Pb^{(Q-1)+}$ beam created because of electron capture by circulating $Pb^{(Q)+}$ ions. The measurement revealed a strong counting rate when the scintillator covered the expected position of the recombined ions (in our case 25 mm radially outwards from the circulating beam). The signal was especially strong for a circulating $Pb^{53+}$ beam. A large reduction occurred when the

screen was withdrawn by more than 25 mm from the main beam or when the electron beam was switched off. This indicates that capture of cooling electrons was indeed responsible for the loss, or at least for the major part of it.

The recombination of $Pb^{53}$ is uncomfortably strong and therefore $Pb^{54}$ with 6–10 times longer $\tau_{rec}$ was chosen, for stacking tests as well as for the final scheme.

### 3.7 Beam-induced Pressure Rise

At the higher intensities reached with stacking, a new beam-lifetime problem was encountered. Injecting and accumulating the beam over a longer period, the beam decay rate increased by a large factor. Apparently the loss rate had different contributions: one which was proportional to the 'instantaneous' intensity of the ion beam and another that increased with 'integrated' intensity injected over the last few hours, with a recovery time after the stop of injection, which was also of the order of hours. Both effects were attributed to outgassing of equipment due to the impact of lost ions. In fact the static LEAR vacuum pressure was of the order of $5 \times 10^{-12}$ torr, but local pressure bumps up to $10^{-9}$ torr occurred with 'continuous' multiturn injection of about $10^8$ ions every second. Especially critical was a vertical beam profile monitor, which for reasons of detection efficiency was very close to the beam and which used VESPEL® as insulating material. When this detector was removed and care was taken to avoid losses in other critical places, the life-time with continuous injection finally reached a value of several seconds, long enough to perform stacking tests. However a pressure increase by a factor of five (Figure 14) remained.

This effect will have to be reduced in the project for the LHC by careful choice and treatment of the material for the vacuum chamber and the equipment exposed to the beam in LEIR. For instance the large pressure bump (see Figure 14) at the entrance of section SS4 (present also under static but especially pronounced under dynamic conditions) is due to a horizontal profile monitor which contains organic material. This will be replaced by ceramic components which are better suited for ultra-vacuum and less prone to outgassing under ion impact.

Analysis of the gas composition showed variations around the ring, but a mass-28 component (CO) was responsible for a large fraction

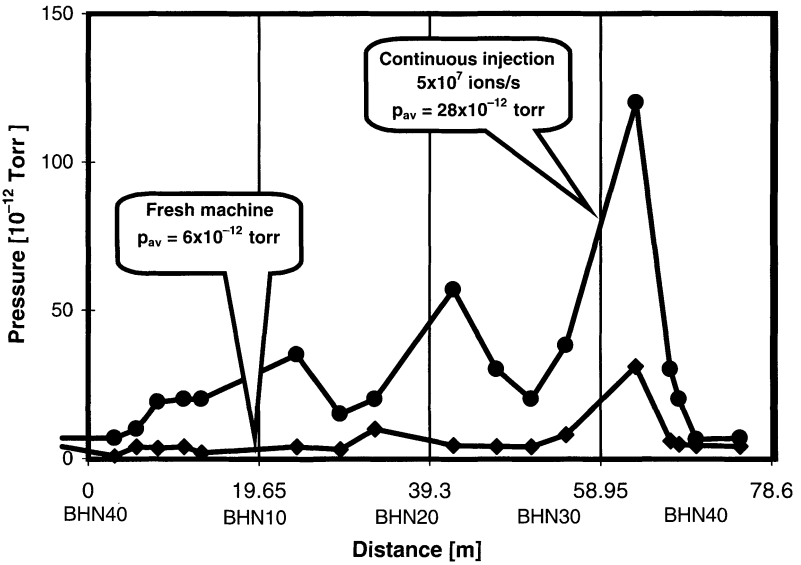


FIGURE 14 Residual gas pressure for the 'fresh' machine and equilibrium with continuous injection of about $5 \times 10^7$ $Pb^{54+}$ ions per second.

of the pressure increase at all locations. Beam-induced desorption of molecules absorbed on the chamber surface has already been encountered in the ISR[28] and intensity-dependent losses from a circulating beam of gold ions have recently been observed at the booster of the Brookhaven AGS.[29] In the ISR the effect could be strongly reduced by higher bake-out temperatures and/or special cleaning methods (argon-glow discharge), together with improved pumping.[28,30]

## 4 MULTITURN INJECTION AND STACKING TESTS

### 4.1 Setting up for Multi-injection

After the reconfiguration of LEAR (Figure 2), multiturn injection and stacking were investigated in a programme of experiments during a five-month period in 1997. The repetition time of the lead-ion linac was shortened to 0.4 s and the ramping of the linac momentum was made operational for the experiments. A series of pre-tests was necessary to commission the new hardware and new settings.

To test the novel optics for the transfer line, $Pb^{53+}$ and $Pb^{54+}$ ions were simultaneously transmitted. To this end the magnetic filter line after the stripping foil was adjusted for a large momentum width ($> 2\%$). After fine-tuning of the transfer line both beams passed and the two beam spots on a scintillation screen in front of the LEAR septum were superimposed with good accuracy (Figure 15). This proves that the

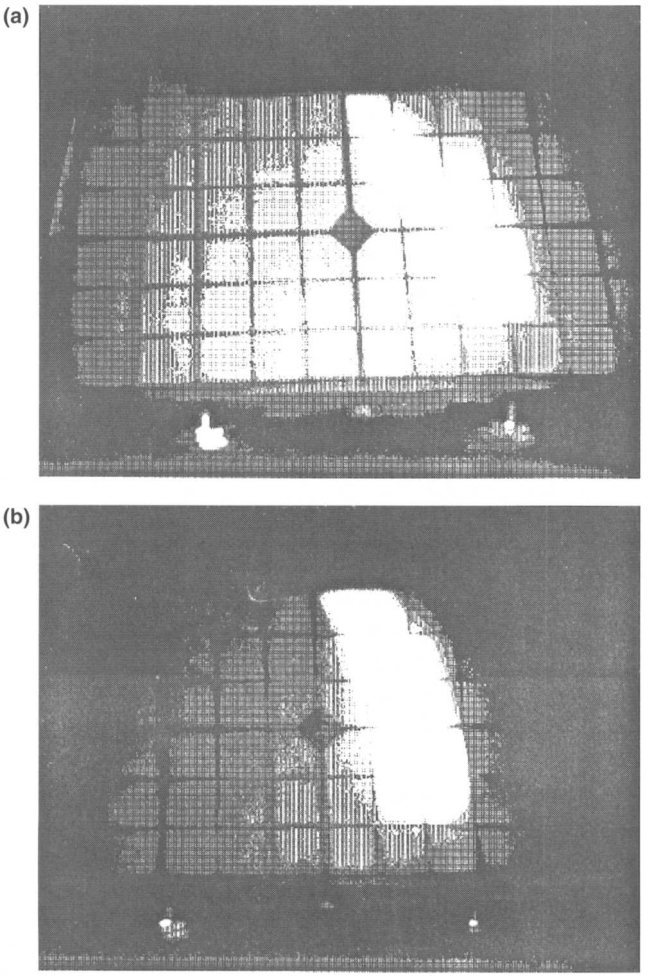


FIGURE 15 Image on a scintillator screen after the septum, when a $Pb^{53+}$ and a $Pb^{54+}$ beam are simultaneously transferred; (a) with calculated settings, (b) with best settings found for correction of the horizontal dispersion of the transfer line.

momentum acceptance of the line was larger than $18 \times 10^{-3}$ and the residual dispersion at the septum was small as required.

To set up the ramping of the linac momentum, optimum settings for some different energies were found 'statically' by changing the RF amplitude of tank 3 and choosing the debuncher phase which gave the best beam density (high intensity and small momentum spread) for the corresponding momentum. In this optimization, the LEAR ring with monoturn injection was used as a 'spectrometer' by observing the momentum distribution, and the intensity, from the longitudinal Schottky scan (Figure 16). In this way, the functions $U_{\text{tank3}}$ ($p_{\text{L}}$) and $\phi_{\text{debuncher}}$ ($p_{\text{L}}$) were established and the function generators were programmed accordingly to generate an approximately linear ramp with a $\Delta p/p_{\text{L}}$ increasing up to $8 \times 10^{-3}$ in a time that could be chosen between 50 and 200 μs (Figure 17). For most of the tests a ramp of $\leq 6 \times 10^{-3}$ in 200 μs was used.

The injection into LEAR was optimized 'statically' for different momentum slices by shortening the linac pulse to about 10 μs (4–5 turns in LEAR). Changing the timing of the ramp, the injected momentum

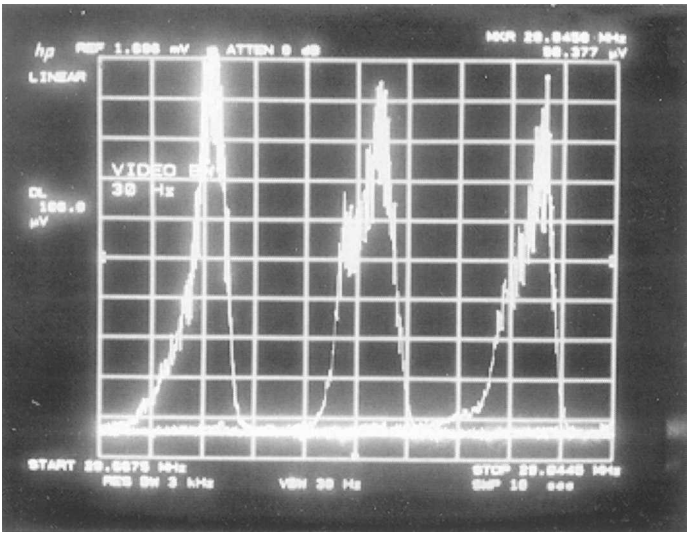


FIGURE 16 Momentum distribution for three different linac momenta: $-3 \times 10^{-3}$, 0, and $+3 \times 10^{-3}$, corresponding roughly to the beginning, the centre and the end of the ramp.

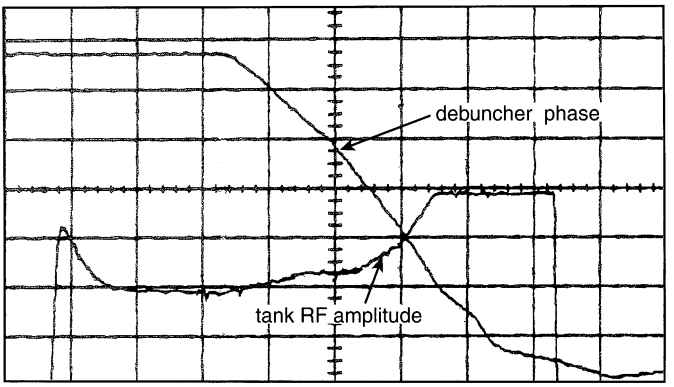


FIGURE 17 Debuncher phase and RF amplitude of tank 3 to create the linear momentum ramp of the linac beam. Scales: horizontal 50 μs/div., vertical 10°/div. and ~ 1 kV/div.

could be chosen. Then by adjusting the timing of the bump, the multiturn injection for the given slice was optimized with the constraint that the transverse emittance did not exceed $50\pi$ mm mrad. In this way the relation between linac energy and orbit bump was established and the bump generators could be programmed accordingly. In this procedure the momentum distribution was again observed via Schottky noise scans and the transverse emittances were viewed with the beam ionization profile monitors. In most of the experiments, an orbit bump of 40 mm, collapsing in 200 μs was used. A relatively uniform filling over a momentum width of $\pm 3 \times 10^{-3}$ (Figure 18) was obtained in this way.

The setting up of each new optics required a series of precision measurements and adjustments. At the start the theoretical currents were set. Using the LEAR tune-measurement and tune-correction system, $Q_h$ and $Q_v$ were adjusted with a precision of 0.001 via the main quadrupole currents. The dispersion was checked by tracking an off-momentum beam with the help of 16 position pickup electrodes around the ring (Figure 19). Fine adjustment of $D$ was achieved via the currents of the trim supplies. A detailed verification of the optics was then made by measuring the horizontal and vertical betatron phase advance between adjacent pairs of pickups (Figure 20). For this measurement a digital network analyser was used to determine the Beam Transfer Function (BTF) from a fixed-loop coupler kicker to the two pickups (Figure 21). For high accuracy, the BTF phases were measured at the

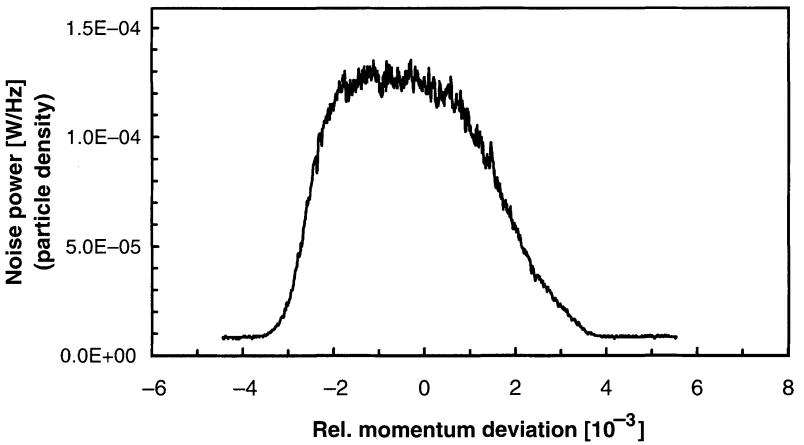


FIGURE 18 Momentum distribution (spectral power density of Schottky noise around a harmonic of the revolution frequency) of the beam after a combined longitudinal and horizontal multiturn injection. The instantaneous momentum spread of the linac beam $(\sigma_p/p)$ is about $2.5 \times 10^{-4}$

first 51 betatron sidebands $(n \pm Q)f_{\text{rev}}$ (i.e. over the whole range of 0.1–20 MHz) and averaged. Then the closed orbit was corrected with special weight on the orbit in the cooling section, and the bump for multiturn injection was set up. Originally carried out with protons, the tuning up of a 'new machine' became possible with lead ions, when the multiturn injection had lead to a sufficient intensity.

## 4.2 Tests of the Combined Horizontal and Longitudinal Multiturn Injection

The stacking tests were mainly performed with the machine 97-0 with $D \approx 10\,\text{m}$, $\beta_{\text{H}} \approx 4\,\text{m}$ in the injection region. Adjusting the orbit bump to decrease from 40 mm to zero in 200 μs while the linac momentum increased by $4 \times 10^{-3}$, up to $1.5 \times 10^8$ ions per injection (corresponding to about 30 effective turns), could be captured in the machine within a horizontal emittance $(2\sigma)$ of $50\pi$ mm mrad. This is not too far from the value of 25 efficient turns calculated in Ref. [14] under the assumption of 40% loss. A comparative test was also performed with machine 1 and for this case an intensity limit of $1.1 \times 10^8$ ions per injection (22 effective turns) was found with combined horizontal and longitudinal injection. This has to be compared to a classical, purely horizontal multiturn

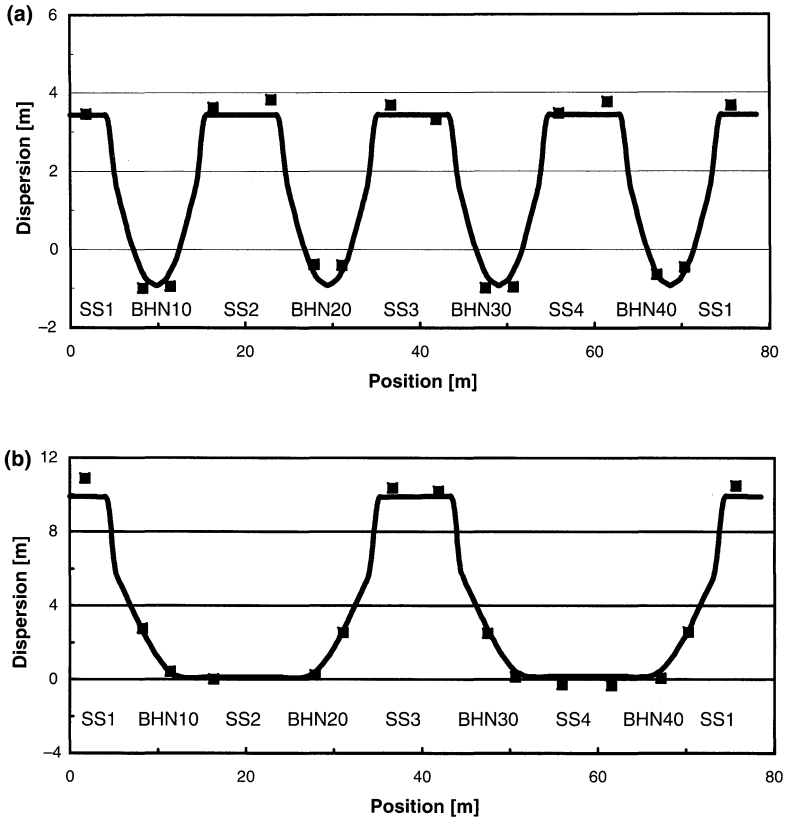


FIGURE 19 Dispersion around machine 1 and machine 97-0. Theoretical curves and points measured.

scheme, which loses a factor of 2 to 3 in the injected intensity even if one uses up the full acceptance of $150\pi$ mm mrad.[14]

### 4.3 Multi-injection and Stacking with Electron Cooling

In the final scheme about 10 batches of $1-2 \times 10^8$ ions resulting from each injection have to be stacked in 1 s with the linac pulsing at 10 Hz repetition rate. In the experiments, two different stacking procedures were tried out with the linac repetition rate of 2.5 Hz. The first one uses electron cooling matched to the velocity of the stack, i.e. with a fixed $\Delta p/p = -2 \times 10^{-3}$ with respect to the central momentum (centre of the

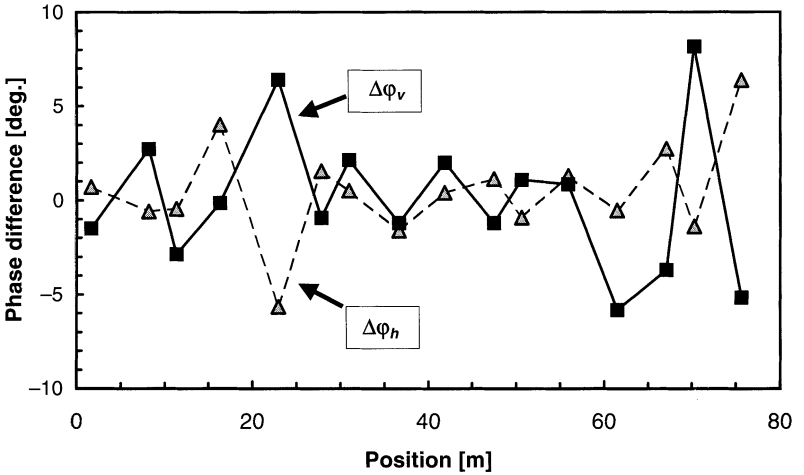


FIGURE 20 Example of the phase advance (difference of theoretical and measured value) between adjacent pairs of pickup electrodes.

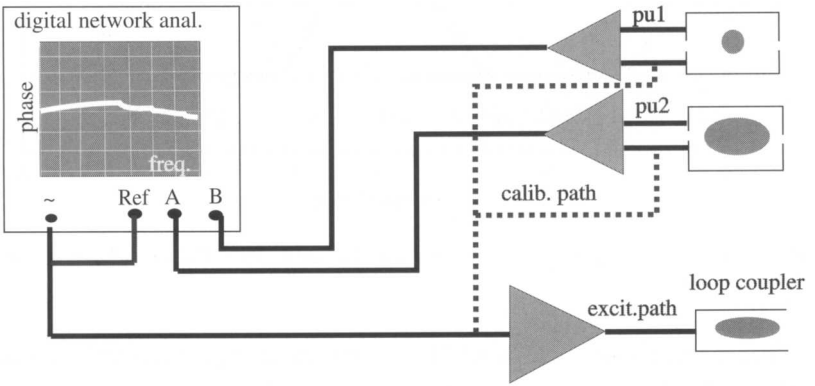


FIGURE 21 Principle of the set-up to measure the phase advance between two pickups.

chamber). Thus the stack sits at the bottom of the electron velocity parabola (Figure 10(c)) and the newly injected particles are decelerated and cooled into the stack 'from above' with a large initial velocity difference to the electrons. This scheme is most efficient with a finite (but not too large) dispersion function in the cooling section, which improves the velocity matching as discussed in Section 3.3.

In the second procedure, the electron velocity is changed prior to each new injection to match the central momentum of the injected beam. After about 150 ms it is then slowly (200 ms) dragged back to $\Delta p/p = -2 \times 10^{-3}$, the 'parking value' of the stack. This second scheme is better adapted to zero dispersion at the cooler. With finite dispersion the horizontal position of the electron (or ion) beam has to be swept together with the energy of the electrons in order to provide good velocity matching in the presence of space charge.

Three different situations were tested: machine 97-0 without and with energy sweeping and machine 1 without sweeping. Results for the first case are displayed in Figure 22. One notes that after 12 injections of $1-1.5 \times 10^8$ ions, about $6 \times 10^8$ ions are accumulated with peaks reaching $7 \times 10^8$. At this intensity level the stacking process saturates because the losses during the interval between consecutive injections balance the number of particles added per injection. With a loss rate $1/\tau$, and the linac cycling rate $1/t_{\text{linac}}$, one expects a stacking factor given by:

$$N_{\text{stack}}/N_{\text{inj}} = [1 - \exp(-t_{\text{linac}}/\tau)]^{-1}.$$

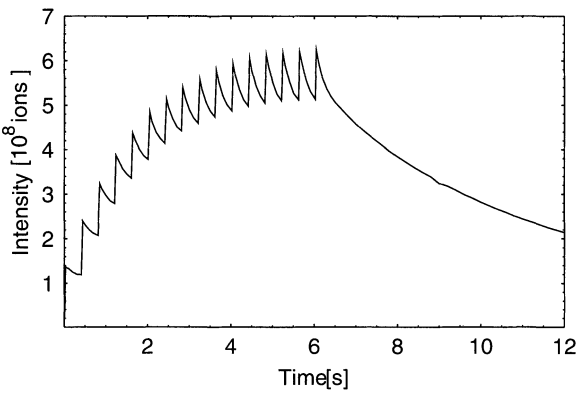


FIGURE 22 Accumulation of lead ions with electron cooling: Every 0.4 s about $1 \times 10^8$ ions are added by multiturn injection. After 4 s an intensity of $6 \times 10^8$ ions is attained and saturation is reached. After the stop of the injection, the beam lifetime is 6.5 s. The electron cooling was with a current of 0.105 A and the electron energy was at a fixed value corresponding to the stack momentum ($\Delta p/p = -3 \times 10^{-3}$ with respect to the central momentum of the machine).

With $t_{\text{linac}} = 0.4$ s the saturation at a stacking factor of about 7 indicates an effective life-time of $\tau \approx 2.6$ s only. Part of the loss can be accounted for by a beam halo, which is not sufficiently cooled before the new injection takes place. Another part is probably explained by the increased charge exchange due to outgassing caused by injection losses. In fact in Figure 23, which displays the mass-28 (CO) signal of a gas analyser in SS2, one notes an increase of the partial pressure at each injection. When the injection was stopped, or when a screen was inserted in the transfer line to prevent the arrival of new particles, the beam life increased to 6 s, even when the orbit bump was left operational.

No clear improvement was obtained with energy sweeping. The overall results for machine 1 (and no sweeping) were only slightly less favourable: about $5 \times 10^8$ ions accumulated with peaks of $6 \times 10^8$. The cooling and stacking for machine 1 were as efficient, maybe even slightly better, but the intensity at each multiturn injection was less, as explained in Section 4.2.

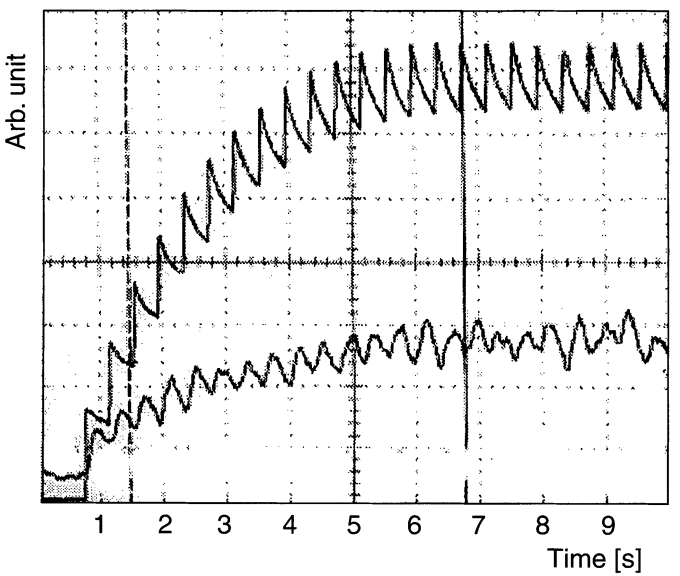


FIGURE 23 Ion-beam current (upper curve) and CO partial pressure (lower curve) during accumulation of about $5 \times 10^8$ $Pb^{54+}$ ions. The peak CO pressure (at the analyser in straight Section 4) rises to about $5 \times 10^{-12}$ torr.

All stacking results so far are for 100 mA electron current and the cooling length of 3 m ($\eta_{\text{cool}} \approx 0.4$). For larger currents, smaller beam dimensions were measured, leading to reduced losses at the next injection, but stronger losses occurred during cooling.

### 4.4 High-intensity Effects

The transverse feedback system of LEAR, with a bandwidth of 70 MHz, which acts on the first 190 transverse modes, was needed to stabilize the high-density stack. When this system was well adjusted, and the electron cooling was stable, any sign of transverse instabilities disappeared. Longitudinal instabilities and other space–charge effects of the ion beam were usually of no concern. However when 'jumps' in the energy of the electron cooling due to insufficient control of the neutralization or other 'discontinuities' in the electron beam occurred, losses and signs of instability were observed. These could only be avoided by strict 'quality control' of the electron beam (as discussed in Section 3.4 above).

The main problem at high intensity remains the reduction of the beam life-time due to beam-induced outgassing of CO and probably other gases as discussed above.

## 5 CONCLUSIONS

The experiments show the feasibility of the proposed stacking scheme and its potential to reach ion-beam densities above LHC requirements. A gain of more than 100 in intensity and density has been demonstrated. The performance already reached in the test is only a factor of two short in the intensity and another factor of two in the stacking rate required. Substantial improvements are possible by a number of measures: upgrade of the ECR source, multiturn injection into all three phase planes, state-of-the-art electron cooling, storage-ring optics with optimum betatron and dispersion functions. The vacuum and particularly ways to control the beam-induced outgassing are of special importance. Methods of surface treatment developed at the CERN-ISR look promising for this purpose and careful choices of the materials exposed to the vacuum are mandatory. The recombination problem can be circumvented by the selection of a suitable charge state.

## *References*


[1] The LHC Study Group, P. Lefevre and T. Pettersson (Eds.), The Large Hadron Collider, conceptual design, CERN/AC/95-05 (LHC).

[2] The ALICE Collaboration, Technical proposal for A Large Ion Collider Experiment at the CERN LHC, CERN/LHCC 95-71.

[3] P. Lefèvre and D. Möhl, A low energy accumulation ring of ions for LHC (a feasibility study), CERN/PS 93-62 (DI) 1993, *Proc. Workshop on Beam Cooling*, Montreux, 1993, J. Bosser (Ed.), CERN 94-03, p. 411; D. Brandt, E. Brouzet, R. Cappi, J. Gareyte, R. Garoby, H. Haseroth, P. Lefèvre, S. Maury, D. Möhl, F. Pedersen, K. Schindl, T.R. Sherwood, L. Thorndahl and D. Warner, High intensity options for the CERN heavy ion programme, CERN/PS 90-20 (DI), *Proc. 1990 European Particle Accelerator Conference*, Nice, 1990, p. 49.

[4] LEAR Design Study Group, G. Plass (Ed.), Design study of a facility for experiments with low energy antiprotons, CERN/PS/DL 80-7.

[5] D. Warner (Ed.), CERN Heavy-ion facility design report, CERN 93-01.

[6] H. Haseroth, A heavy ion injector at CERN, CERN/PS 90-63 (DI), *Proc. 1990 Linac Conference*, Albuquerque, USA, 1990, p. 568.

[7] J. Bosser, R. Lapik, R. Ley, I. Meshkov, V. Poliakov, E. Seleznev, A. Smirnov, E. Syresin, G. Tranquille, A. Zapunjakov and M. Zavzraznov, The variable current gun: the parameter tests and results of first electron cooling experiments at LEAR, *Nucl. Instrum. Methods A*, **355**, 1995, 208.

[8] R. Maccaferri, Ecool momentum feedback control and operation, internal report, CERN/PS/AR Note 95-07.

[9] J. Bosser, A review of recent work on electron cooling at LEAR, *Proc. Workshop on Crystalline Beams and Related Topics 1995*, A.G. Ruggiero (Ed.), World Scientific, 1996, p. 435; J. Bosser, R. Ley, I. Meshkov, G. Molinari, V. Polyakov, A. Smirnov, E. Syresin, G. Tranquille and F. Varenne, Electron cooling with neutralised electron beams, *Proc. 1994 European Particle Accelerator Conference*, London, p. 1211; F. Varenne, Neutralisation de la charge d'espace du faisceau d'électrons du refroidisseur électronique de LEAR, Doctoral thesis, University of Clermont-Ferrand (France), Nov. 1995, Reprint: Internal report CERN/PS/AR Note 96-22; I. Meskov, D. Möhl, G. Tranquille and E. Syresin (Eds.), Neutralisation of the electron-beam space charge, report of the CERN/PS/JINR/ITEP 1994–95 collaboration, internal report CERN/PS/DI Note 98-16.

[10] C. Carli, LEAR lattices for ion accumulation, Internal report CERN/PS/DI Note 96-22.

[11] S. Maury and D. Möhl, Combined longitudinal and transverse multiturn injection into a heavy ion accumulator ring, Internal report CERN/PS/AR Note 94-12; C. Carli, S. Maury and D. Möhl, Combined longitudinal and transverse multiturn injection in a heavy ion accumulator ring, *Proc. 1997 Particle Accelerator Conference*, Vancouver, p. 976.

[12] C. Prior and H. Schönauer, Multiturn injection into accumulators for heavy ion inertial fusion, *Proc. 1996 European Particle Accelerator Conference*, Sitges (Spain), p. 2391.

[13] K. Schindl and P. van der Stok, A method for increasing the multiturn injection efficiency in A.G. synchrotrons by means of skew quadrupoles, *Proc. 1977 Particle Accelerator Conference*, *IEEE Trans. Nucl. Sci.*, **NS-24**(3), 1977, 1390; P. van der Stok, Multiturn injection into the CERN Proton Synchrotron Booster (Doctoral thesis), Internal report CERN/PS/BR 81-28.

[14] C. Carli, Simulation of multiturn injection into LEAR in view of ion accumulation, Internal report CERN/PS/DI Note 96-24.

[15] C. Carli, Beam transfer line optics for the lead ion cooling and accumulation tests in LEAR, Internal report CERN/PS/DI Note 97-3.

[16] A. Fowler and K.D. Metzmacher, The injection bumper system for LEIR ion tests, Internal report CERN/PS/CA Note 98-22; M. Chanel, S. Maury and D. Möhl, Specification of a LEAR bump for multiturn injection, Internal report CERN/PS/AR Note 96-4.
[17] M. Chanel and G. Molinari, Beam Ionisation Profile Monitor (BIPM) to measure beam profiles in LEAR (to be published).
[18] G. Tranquille, A general purpose PC based data acquisition system, *Proc. 1996 Workshop on Personal Computers and Particle Accelerator Controls* (*PCaPAC*), *DESY*, Hamburg, October 1996.
[19] J. Bosser, J. Broere, C. Carli, M. Chanel, C. Hill, R. Ley, A. Lombardi, R. Maccaferi, S. Maury, D. Möhl, G. Molinari, H. Mulder, E. Tanke and G. Tranquille, LEAR Machine studies to test ion accumulation for the LHC, Summary March–April 1996, Internal report CERN/PS/AR Note 96-09.
[20] J. Bosser, G. Tranquille and I. Meshkov, Magnetized electron beam cooling time for heavy ions, Internal report CERN/PS/AR Note 94-11.
[21] A. Burov, V. Kudelainen, V. Lebedev, V. Parkhomchuk, A. Sery and V. Shiltsev, Experimental study of an electron beam in compensated state, Novosibirsk report, Engl. trans.: Internal report CERN/PS 93-08(AR); J. Bosser, I. Meshkov, D. Möhl, V. Parkhomchuk, E. Syresin and G. Tranquille, Neutralization of the LEAR-ECOOL electron beam space charge, Internal report CERN/PS/AR Note 93-08; G. Tranquille, Suppression of natural neutralisation of the electron beam space charge via polarised tubes, Internal report CERN/PS/OP Note 95-47.
[22] J. Bosser, Influence of neutralization on electron transverse velocity, Internal report CERN/PS/BD Note 98-01.
[23] Experiments performed by M. Chanel, R. Ley and G. Tranquille. A description is given in: E. Mustafin and D. Möhl, The distribution of the neutralizing ions in the LEAR electron cooling system, Internal report CERN/PS/DI Note 97-18.
[24] R. Maccaferri, Ion clearing by RF-shaking (to be published); See also Ref. [9] above.
[25] B. Franzke, Vacuum requirements for heavy ion synchrotrons, *Proc. 1981 Particle Accelerator Conference*, *IEEE Trans. Nucl. Sci.*, **NS-28**(3), 1981, 2116.
[26] S. Baird, J. Bosser, C. Carli, M. Chanel, P. Lefevre, R. Ley, R. Maccaferi, I. Meshkov, D. Möhl, G. Molinary, F. Motsch, G. Tranquille and F. Varenne, Measurement of the life-time of Pb52+, Pb53+ and Pb54+ beams at 4.2 MeV per nucleon subject to electron cooling, *Phys. Lett.*, **B361**, 1995, 184.
[27] O. Uwira, A. Möller, J. Linkemann, T. Bartsch, C. Brandau, M. Schmitt, A. Wolf, D. Schwalm, R. Schuch, W. Zog, H. Lebius, W.G. Graham, J. Doefert and D.W. Savin, Recombination measurements at low energies with Au49+, 50+, 51+ at the TSR, *Hyperfine Interact.*, **108**, 1997, 149.
[28] R. Calder and O. Gröbner, Beam induced gas desorption in the CERN Intersecting Storage Rings, *Proc. 1973 Particle Accelerator Conference*, *IEEE Trans. Nucl. Sci.*, **NS-20**, 1973, 760.
[29] M. Blaskiewicz, L. Ahrens and H. Calvi, Anomalous, intensity dependent losses in Au(32+) beams, *Proc. 1997 Particle Accelerator Conference*, Vancouver p. 959.
[30] R. Calder and O. Gröbner, Desorption coefficient of the vacuum test chambers, Internal report CERN-ISR Performance Report ISR VA/OG/nb 26 Nov. 1974.